Preconditioned multiple-relaxation-time lattice Boltzmann equation model for incompressible flow in porous media

Xuhui Meng,[1,2] Liang Wang,[3] Xiaofan Yang,[1,2,*] and Zhaoli Guo[4,2,†]

[1]*State Key Laboratory of Earth Surface Processes and Resource Ecology, Faculty of Geographical Science, Beijing Normal University, Beijing 100875, China*

[2]*Beijing Computational Science Research Center, Beijing 100193, China*

[3]*Research Center of Engineering Thermophysics, North China Electric Power University, Beijing 102206, China*

[4]*State Key Laboratory of Coal Combustion, Huazhong University of Science and Technology, Wuhan 430074, China*

(Received 25 June 2018; published 27 November 2018)

An improved preconditioned multiple-relaxation-time lattice Boltzmann equation model for incompressible flow (IPMRT-LBE) in porous media is proposed. Motivated by previous LBE models [Guo *et al.*, Phys. Rev. E **70**, 066706 (2004); Premnath *et al.*, J. Comput. Phys. **228**, 746 (2009); Guo *et al.*, J. Comput. Phys. **165**, 288 (2000)], the current model is demonstrated to have the advantages of accurate implementation of the no-slip boundary condition, reducing the compressible effect as well as fast convergence rate compared with standard LBE models. To validate the IPMRT-LBE model, flows in two- and three-dimensional synthetic porous media (square array of cylinders and body-centered cubic array of spheres) are simulated. The results show that the current model can predict the macroscopic property (such as permeability) accurately with significantly accelerated convergence rate. Furthermore, simulations of flow through a three-dimensional sandpack confirm the applicability and advantages of the IPMRT-LBE model.

DOI: 10.1103/PhysRevE.98.053309

I. INTRODUCTION

Flow and transport in porous media are fundamental processes but critical in many environmental and industrial applications, such as contaminant transport in groundwater, oil recovery, CO_2 sequestration, and so on. Accurate descriptions of such processes, especially small-scale mechanisms and their impact factors (such as heterogeneity, surface precipitation and dissolution, etc.), are thus important to advance our understanding of large-scale system behaviors. However, it is difficult to fully capture microscopic (e.g., pore-scale) features by using the macroscopic (e.g., Darcy-scale) approach. With the fast development of computational algorithms and computing resources, pore-scale direct numerical simulations (DNS) have become feasible to investigate flow and transport processes in synthetic and engineered porous media systems [1,2].

Pore-scale flows can be described by the steady-state incompressible Navier-Stokes (NS) equations with low Reynolds numbers (Re $\ll$ 1) [1,3–5]. Even though the transient terms in the NS equations can be ignored [5], analytical solutions are still difficult to obtain due to the complexity of the equations as well as the pore morphology. In recent decades, much effort has been taken into developing DNS to solve the unsteady and steady NS equations. Classified in two catogories, there are conventional grid-based models [e.g., the finite-difference method (FDM), finite-volume method (FVM), etc.], and particle-based models [e.g., the lattice Boltzmann method (LBM) and smoothed particle hydrodynamics (SPH)] [5–9]. However, most DNS methods (especially grid-based) have trouble treating complex pore structures, which has limited their applications in simulating flow and transport in porous media [1,3].

The lattice Boltzmann equation (LBE) model, which is favored for its easy treatment of complex boundaries, has been widely used for simulating pore-scale transport processes [1,3,4,10,11]. By far, a series of LBE models have been developed for various purposes, such as miscible flows, natural convection, non-Newtonian flows, and so on [3,12–15]. Unfortunately, as reported in Refs. [16–18], most of the existing LBE models suffer from slow convergence even for steady flows due to the fact that the models are numerically explicit, which prevents them from practical applications. To overcome this problem, there have been specific LBE models developed targeting at fast convergence rate compared with standard LBE models [19–22]. Nevertheless, these methods often employ complicated algorithms [18], which are cumbersome to implement, especially for objects with complex geometries, and thus not quite suitable for simulating pore-scale flows. For the past decade, progresses have been made to accelerate the convergence of the standard LBE model while keeping its simplicity. Guo *et al.* proposed a preconditioned single-relaxation-time LBE model (PSRT-LBE) for steady NS equations by including a preconditioning factor in the equilibrium distribution functions (EDFs) [18]. By adjusting the preconditioning parameter, one can enlarge the effective Mach number as well as the relaxation times, both of which can significantly accelerate the convergence rate. Since the PSRT-LBE only modified the EDFs by incorporating one factor, it retains the same simplicity as the standard LBE mod-

*Corresponding author: xfyang@bnu.edu.cn

†Corresponding author: zlguo@hust.edu.cn

els. However, as pointed out in Refs. [3,23], for simulating porous media flows, LBE models with single-relaxation-time collision term (SRT-LBE) have the defect that the computed permeability increases with the fluid viscosity due to the incorrect implementation of the no-slip boundary condition at the fluid-solid interface. This weakness may be overcome by using the multiple-relaxation-time collision model (MRT-LBE) if the relaxation times are specifically determined [3,23]. Most recently, Premnah *et al.* introduced a preconditioned multiple-relaxation-time lattice Boltzmann equation (PMRT-LBE) model on the basis of the PSRT-LBE to achieve a better numerical stability [24], although it is noted that the relaxation times, which are crucial for accurately implementing no-slip boundary conditions, were not carefully derived in the PMRT-LBE but using arbitrary values [24]. In other words, if used for permeability computations, both the PSRT-LBE and PMRT-LBE cannot eliminate the defect of viscosity-dependent permeability. What's more, it is noted that the fluid density is related to the pressure in both models, suggesting that the fluid density will change due to the variation of the pressure even for incompressible flows (i.e., compressible effect) [3,18]. Therefore, computational errors may be introduced in simulating incompressible flows with pressure variations. As known, in simulating flow in porous media, the pressure field usually changes dramatically due to the complex pore structures, indicating that these two models may not be suitable for such applications [25]. Therefore, to accurately and efficiently simulate low-speed incompressible flow in porous media and predict macroscopic properties, LBE models with fast convergence rate and precise treatments of no-slip boundary condition are still desirable and remain challenged.

In the present work, we aim to propose a preconditioned multiple-relaxation-time lattice Boltzmann equation model for incompressible flow in porous media (IPMRT-LBE), which is expected to be accurate, efficient, and relatively easy to implement. The rest of the paper is organized as follows. The proposed IPMRT-LBE model is explained in Sec. II, with validations, applications, and discussions in Sec. III. Finally, a brief summary is given in Sec. IV.

II. MODEL DEVELOPMENT

A. Governing equations

Flow in porous media at the pore scale are generally described by the incompressible Navier-Stokes equations as follows:

$$\begin{aligned} \nabla \cdot \boldsymbol{u} &= 0, \\ \partial_t \boldsymbol{u} + \boldsymbol{u} \cdot \nabla \boldsymbol{u} &= -\nabla P + \nu \nabla^2 \boldsymbol{u} + \boldsymbol{F}, \end{aligned} \tag{1}$$

where $\boldsymbol{u}$ is the velocity vector [i.e., $\boldsymbol{u} = (u, v)$ in two dimensions and $\boldsymbol{u} = (u, v, w)$ in three dimensions], P denotes the pressure divided by the fluid density, ν is the kinetic viscosity, and $\boldsymbol{F}$ is the acceleration caused by the body force (e.g., gravity). As mentioned in the Introduction (Sec. I), transient terms [time derivatives in Eq. (1)] as well as the convective term $\boldsymbol{u} \cdot \nabla \boldsymbol{u}$ can be neglected for low Reynolds number flows in porous media.

B. Preconditioned multiple-relaxation-time lattice Boltzmann equation

In the lattice Boltzmann method (LBM), the space is discretized into regular lattices. All distribution functions are assumed to move with a series of discrete velocities on these nodes. In two dimensions (2D), the most popular discrete velocity model is D2Q9 (two-dimension-nine-velocity), which is defined as

$$\boldsymbol{c}_i = \begin{cases} c(0,0), & i = 0, \\ c(\cos[(i-1)\pi/2], \sin[(i-1)\pi/2]), & i = 1, \ldots, 4, \\ 2c(\cos[(i-5)\pi/2 + \pi/4], \sin[(i-5)\pi/2 + \pi/4]), & i = 5, \ldots, 8, \end{cases} \tag{2}$$

where $c = \delta_x/\delta_t$ is the lattice speed and δ_x and δ_t are the lattice spacing and time step, respectively. In addition, the D3Q19 (three-dimension-nineteen-velocity) model is mostly used in three-dimensional scenarios, which are expressed as

$$\boldsymbol{c}_i = \begin{cases} c(0,0,0), & i = 0, \\ c(\pm 1,0,0), c(0,\pm,0), c(0,0,\pm 1), & i = 1, \ldots, 6, \\ c(\pm 1,\pm 1,0), c(\pm 1,0,\pm 1), c(0,\pm 1,\pm 1), & i = 7, \ldots, 18. \end{cases} \tag{3}$$

As in the standard LBE models, the evolution equation in the present IPMRT-LBE model reads as

$$\boldsymbol{f}(\boldsymbol{x} + \boldsymbol{c}\delta_t, t + \delta_t) - \boldsymbol{f}(\boldsymbol{x}, t) = -(\boldsymbol{M}^{-1}\boldsymbol{S})[\boldsymbol{m}(\boldsymbol{x}, t) - \boldsymbol{m}^{\mathrm{eq}}(\boldsymbol{x}, t)] + \delta_t \hat{\boldsymbol{F}}, \tag{4}$$

where $\boldsymbol{f}(\boldsymbol{x}, t)$ is the particle distribution function (PDF) at position $\boldsymbol{x}$ and time t with velocity $\boldsymbol{c}$ for the velocity space, while $\boldsymbol{m}$ is the PDF at the moment space. $\boldsymbol{M}$ is the transformation matrix, which maps $\boldsymbol{f}$ to $\boldsymbol{m}$ as $\boldsymbol{m} = \boldsymbol{M} \cdot \boldsymbol{f}$. In addition, $\boldsymbol{S} = \mathrm{diag}[s_0, \ldots, s_{b-1}]$ is the diagonal relaxation factor matrix, where b is the number of the discrete velocities and $\boldsymbol{m}^{\mathrm{eq}}(\boldsymbol{x}, t)$ is the equilibrium distribution function (EDF) at the moment space.

To accelerate the convergence rate of the present model, the preconditioning employed in the PSRT-LBE [18] is also adopted here by introducing a preconditioning factor (γ) in the EDF. Futhermore, to reduce the compressible effect of the PSRT-LBE and PMRT-LBE models, we derive a new formulation of the EDF based on the incompressible LBE model developed in Ref. [26]. For the D2Q9 and D3Q19 models, respectively, the new EDFs are expressed as

$$\boldsymbol{m}^{\mathrm{eq}} = (0, e, \varepsilon, j_x, q_x, j_y, q_y, p_{xx}, p_{xy})^T = \left(0, 6P + \frac{3\boldsymbol{u}^2}{\gamma}, -9P - \frac{3\boldsymbol{u}^2}{\gamma}, u, -u, v, -v, \frac{u^2 - v^2}{\gamma}, \frac{uv}{\gamma}\right)^T \tag{5}$$

and

$$\begin{aligned}\boldsymbol{m}^{\mathrm{eq}} &= (0, e, \varepsilon, j_x, q_x, j_y, q_y, j_z, q_z, 3p_{xx}, 3pi_{xx}, p_{ww}, p_{xy}, p_{yz}, p_{xz}, m_x, m_y, m_z)^T \\ &= \left(0, 57P + \frac{19\boldsymbol{u}^2}{\gamma}, -27P - \frac{11}{2}\frac{\boldsymbol{u}^2}{\gamma}, u, -\frac{2}{3}u, v, -\frac{2}{3}v, w, -\frac{2}{3}w, \frac{2u^2 - v^2 - w^2}{\gamma},\right. \\ &\quad \left.\frac{-2u^2 + v^2 + w^2}{2\gamma}, \frac{v^2 - w^2}{\gamma}, \frac{-v^2 + w^2}{2\gamma}, \frac{uv}{\gamma}, \frac{vw}{\gamma}, \frac{uw}{\gamma}, 0, 0, 0\right)^T, \end{aligned} \tag{6}$$

where superscript T denotes the transpose operator. By incorporating the new EDFs, the present IPMRT-LBE model is expected to retain the fast convergence rate of the PSRT-LBE via preconditioning while reducing its compressible effect.

The discrete external force ($\hat{\boldsymbol{F}}$) in the current IPMRT-LBE model can be derived as

$$\hat{\boldsymbol{F}} = \left[0, \frac{6\boldsymbol{u}\cdot\boldsymbol{F}}{\gamma^2}, \frac{-6\boldsymbol{u}\cdot\boldsymbol{F}}{\gamma^2}, \frac{F_x}{\gamma}, \frac{-F_x}{\gamma}, \frac{F_y}{\gamma}, \frac{F_y}{\gamma}, \frac{2(uF_x - vF_y)}{\gamma^2}, \frac{(vF_x + uF_y)}{\gamma^2}\right] \tag{7}$$

and

$$\begin{aligned}\hat{\boldsymbol{F}} = \left[0, \right.& \frac{38\boldsymbol{u}\cdot\boldsymbol{F}}{\gamma^2}, \frac{-11\boldsymbol{u}\cdot\boldsymbol{F}}{\gamma^2}, \frac{F_x}{\gamma}, -\frac{2F_x}{3\gamma}, \frac{F_y}{\gamma}, -\frac{2F_y}{3\gamma}, F_z, -\frac{2F_z}{3\gamma}, \frac{2(2uF_x - vF_y - wF_z)}{\gamma^2}, \\ & \frac{-(2uF_x - vFy - wF_z)}{\gamma^2}, \frac{2(vF_y - wF_z)}{\gamma^2}, \frac{-(vF_y - wF_z)}{\gamma^2}, \frac{vF_x + uF_y}{\gamma^2}, \frac{wF_y + vF_z}{\gamma^2}, \\ & \left.\frac{wF_x + uF_z}{\gamma^2}, 0, 0, 0\right], \end{aligned} \tag{8}$$

for 2D and 3D scenarios, respectively.

The fluid pressure (divided by the fluid density) and velocity in the present model are calculated as

$$\begin{aligned} P &= \frac{c_s^2}{1-\omega_0}\left[\sum_1^{b-1} f_i(\boldsymbol{x}, t) - \frac{\boldsymbol{u}^2}{2\gamma}\right], \\ \boldsymbol{u} &= \sum_1^{b-1} \boldsymbol{c}_i f_i(\boldsymbol{x}, t) + \frac{\delta_t \boldsymbol{F}}{2\gamma}, \end{aligned} \tag{9}$$

where $c_s = c/\sqrt{3}$ and $\omega_0 = 4/9$ and $1/3$ for the D2Q9 and D3Q19 model as the equilibrium distribution function weight coefficient, respectively. It is noted that Eq. (4) can be recovered to the preconditioned NS equations through Chapman-Enskog expansion analysis (refer to Appendix A for more details):

$$\begin{aligned} \nabla\cdot\boldsymbol{u} &= 0, \\ \partial_t\boldsymbol{u} + \frac{1}{\gamma}\boldsymbol{u}\cdot\nabla\boldsymbol{u} &= -\frac{1}{\gamma}\nabla P^* + \frac{1}{\gamma}\nu\nabla^2\boldsymbol{u} + \frac{1}{\gamma}\boldsymbol{F}, \end{aligned} \tag{10}$$

where $P^* = \gamma P$, and

$$\nu = \gamma c_s^2\left(\tau_\nu - \frac{1}{2}\right)\delta_t, \tag{11}$$

where τ_ν is the viscosity-related relaxation time, which is correlated to the relaxation factors as $1/\tau_\nu = s_7 = s_8$ in 2D and $1/\tau_\nu = s_9 = s_{11} = s_{13} = s_{14} = s_{15}$ in 3D. Equation (10) converges to the same solution for steady flows as Eq. (1) according to Ref. [18]. In addition, it should be noted that the pressure in this model is P (numerical) rather than P^* (physical), with a correlation as $P^* = \gamma P$. Finally, c_s in Eq. (9) is the lattice sound speed in standard LBE, while the lattice sound speed in the present model is $\sqrt{\gamma}c_s$ rather than c_s. We can then define an effective lattice sound speed $c_s^* = \sqrt{\gamma}c_s$ [18,24]. As reported in Refs. [18,24], the disparity between the speeds of the acoustic wave and the waves propagating with the fluid velocity can be decreased by adjusting γ, which leads to a fast convergence of the LBE.

The relaxation factors in the MRT-LBE models are crucial to accurately implement the no-slip boundary condition, which would potentially avoid the defect of viscosity-dependent permeability. According to Ref. [27], the viscosity-independent permeability for any porous media flow can be obtained when $\Lambda = (\tau_q - 1/2)(\tau_\nu - 1/2)$ (definition of τ_q can be found in Appendix B) is kept constant as the bounce-back rule is employed. It is noted that the value of Λ for different flows (e.g., steady flow between two straight and inclined walls) can be different [28–30]. However, the specific value of Λ that ensures the accurate implementation of the no-slip boundary condition at the fluid-solid interface for the steady flow between two straight parallel walls is found to work well even in porous media flows [3,23,28–30]. Here we also compute the value of Λ based on the steady flow between two straight parallel walls. Theoretical results show that the choice of relaxation factors ($s_q = s_4 = s_6$ for 2D and $s_q = s_4 = s_6 = s_8$ for 3D) should be carefully derived rather than assigned with arbitrary values since they would directly impact the slip velocities [Eq. (B21) in Appendix B]. Unlike in the PMRT-LBE model, the relaxation factors follow a correlation listed below in the current IPMRT-LBE model ($\Lambda = 3/16$; please refer to Appendix B for more details)

$$s_q = \frac{16\tau_\nu - 8}{8\tau_\nu - 1}. \tag{12}$$

For more details about the choice of Λ in other flows, one can refer to Refs. [23,28–30].

In summary, the present IPMRT-LBE model has two advantages over the previous models: (1) reducing the compressible effect in the PSRT-LBE and PMRT-LBE, and (2) accurately implementing the no-slip boundary condition by numerically specifying certain relaxation factors rather than using arbitrary values in the PMRT-LBE. In addition, the proposed model could still achieve fast convergence while maintaining the simplicity of the algorithm.

III. RESULTS AND DISCUSSIONS

In this section, a series of numerical experiments are conducted to evaluate the performance of the present model. First, flow through a 2D fracture is simulated. The effect of relaxation factors on the accurate implementation of the no-slip boundary condition is then analyzed. Second, flows in both two- and three-dimensional porous media are simulated based on synthetic pore structures. Permeabilities are then computed to compare with previous studies as further validations. Third, numerical simulations of flow through a digital sandpack are performed as an application. The convergence rates for all cases are evaluated.

A. Flow through a 2D fracture

The pressure-driven flow in a 2D fracture (flow between two parallel plates) is simulated here. The computational domain is defined as $-H/2 \leqslant y \leqslant H/2$, $0 \leqslant x \leqslant L$, where $H = 1.0$ and $L = 0.5$. It is noted that all the physical variables are in lattice units through the current study unless they are specially specified. The initial and boundary conditions employed for this case are expressed as follows:

$$\begin{aligned} u(x, y, 0) &= v(x, y, 0) = 0, \\ u(x, -H/2, t) &= u(x, H/2, t) = v(x, -H/2, t) \\ &= v(x, H/2, t) = 0, \\ P(0, y, t) &= P_{\text{in}}, \quad P(L, y, t) = P_{\text{out}}, \end{aligned} \tag{13}$$

where P_{in} and P_{out} are the pressures at the inlet and outlet, respectively. Based on Eq. (13), an analytical solution can be obtained as

$$u(y) = \frac{G}{\nu}\frac{H^2}{2}\left(\frac{y}{H} - \frac{y^2}{H^2}\right), \tag{14}$$

where $G = -\partial P/\partial x$ is the pressure gradient.

In this problem, the dimensionless characteristic parameter, Reynolds number (Re), is defined as $\text{Re} = u_{\max} H/\nu$, where $u_{\max} = GH/8\nu$ is the maximum velocity obtained from Eq. (14). Two different cases, i.e., Re = 0.1 and 1, are simulated here. The computations are conducted on a 16×32 ($L \times H$) uniform lattice. No-slip boundary conditions at the upper and bottom walls are implemented using the halfway bounce-back scheme, while the nonequilibrium extrapolation scheme [31] is employed to treat the boundaries at the inlet and outlet. The convergence criterion in our simulations is defined as

$$E = \frac{\sum_{ij} |\boldsymbol{u}(\boldsymbol{x}, t + 100\delta_t) - \boldsymbol{u}(\boldsymbol{x}, t)|}{\sum_{ij} |\boldsymbol{u}(\boldsymbol{x}, t + 100\delta_t)|} < 10^{-6}. \tag{15}$$

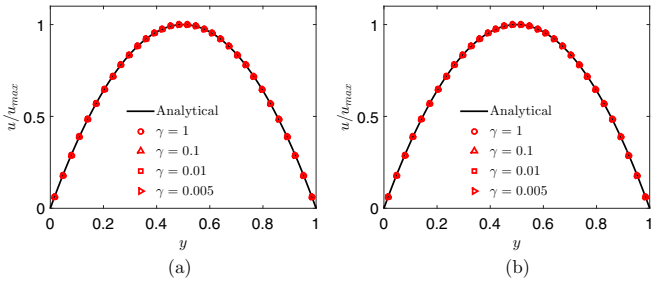

FIG. 1. Flow in 2D fracture: velocity profiles for different preconditioning factors (γ) at two Reynolds numbers. (a) Re = 0.1; (b) Re = 1.

The choices of the relaxation factors used in the 2D fracture simulations include the following: (1) s_1 and s_2, which are validated to have little influence on the numerical results and then specified as 1.0 [3]; (2) $s_0 = 1.0$, $s_3 = s_5 = 0.0$, and $s_7 = s_8 = 1/\tau_\nu$; (3) s_4 and s_6 are calculated by Eq. (12) ($s_4 = s_6 = [16\tau_\nu - 8]/[8\tau_\nu - 1]$) to ensure accurate implementation of the no-slip boundary conditions (Appendix B).

Numerical results of the velocity profiles in the transverse direction are illustrated in Fig. 1, which show good agreement with the analytical solutions for different preconditioning factors (γ) at two Reynolds numbers (Re = 0.1 and 1). To evaluate the impact of γ on the convergence rate, Fig. 2 shows the convergence histories for different γ [the residual error is calculated following Eq. (15)]. It is obvious that the preconditioning ($\gamma < 1$) accelerates the convergence rate as compared with the standard LBE model ($\gamma = 1$). In addition, the smaller the γ, the faster the convergence rate as $\gamma > 0.005$, which is consistent with previous results in Refs. [18,24]. Iteration number for $\gamma = 0.005$ is observed to be larger than those for $\gamma = 0.1$ and 0.01. As shown in Eq. (11), τ_ν increases with the decrease of γ for the same viscosity. Meanwhile, $\tau_q = 1/s_q$ approaches 0.5 with the increase of τ_ν according to Eq. (12). As known, the slow convergence rate as well as the numerical instability will occur as the relaxation times are too close to 0.5 in LBM. Therefore, the iteration number may increase when γ is too small.

To investigate the effect of relaxation factors (s_4 and s_6) on the precise implementation of the no-slip boundary condition, different scenarios are tested in our simulations. For simplicity, we only pick flows at Re = 1 to be the representative. The values of s_4 and s_6 are taken to be arbitrary (0.01, 0.05, 0.5,

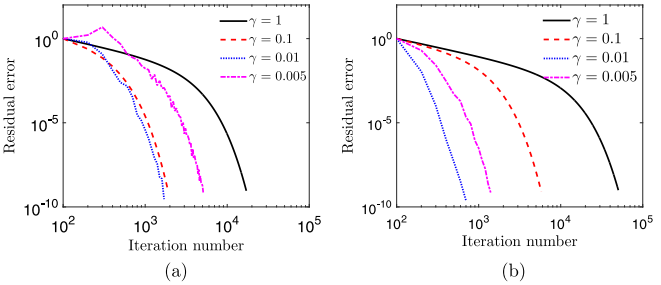

FIG. 2. Flow in 2D fracture: convergence histories for different preconditioning factors (γ) at two Reynolds numbers. (a) Re = 0.1; (b) Re = 1.

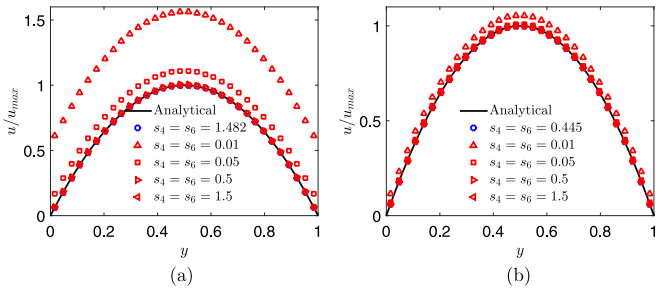

FIG. 3. Flow in 2D fracture: the effect of relaxation factors (s_4/s_6) in the IPMRT-LBE on the velocity profiles. (a) $\gamma = 0.1$; (b) $\gamma = 1$.

1.5) or following the correlation in Eq. (12) (1.482 for $\gamma = 0.1$ and 0.445 for $\gamma = 1.0$). As displayed in Fig. 3, an optimum choice of s_4 and s_6 should be close to the values calculated from Eq. (12). Arbitrary values would lead to unphysical results (slip velocities at the wall boundaries) due to the imprecise implementation of the no-slip boundary condition. Relative errors between simulated results and analytical solution are noticed to increase as the values of $s_4(s_6)$ deviate from those calculated from Eq. (12). In addition, the slip velocity at the wall boundary is found to increase with the decrease of γ. It is reasonable that τ_ν increases with the decrease of γ for the same Reynolds number, leading to a larger slip velocity (more details are shown in Appendix B).

The above results indicate that the present IPMRT-LBE model can achieve faster convergence than standard LBE models by introducing the preconditioning factor while providing accurate results by correctly implementing the no-slip boundary condition at the wall boundaries [selecting the optimum relaxation factors based on Eq. (12)].

Finally, we evaluate the compressible effect using all three models (PSRT-LBE, PMRT-LBE, and the current IPMRT-LBE), which is important to predict macroscopic properties (e.g., permeability) for flow in porous media. Re = 1 is also served as the test case here. The relaxation time in the PSRT-LBE is determined by the fluid viscosity, while the relaxation factors are all set as $s_i = 1.0/\tau_\nu$ in the PMRT-LBE. In the IPMRT-LBE, $s_i = 1.0/\tau_\nu$, $i \neq 4, 6$, while $s_4 = s_6 = [16\tau_\nu - 8]/[8\tau_\nu - 1]$. The computed maximum velocities (normalized by $u_{\max}$ from the analytical solution) are displayed in Table I. As we can see, the maximum velocities calculated by the PSRT-LBE and PMRT-LBE are larger than 1 (especially when $\gamma = 0.01$), which is attributed to the imprecise implementation of the no-slip boundary condition, while the present IPMRT-LBE can provide accurate and consistent results. In addition, the maximum velocities at the outlet in the PSRT-LBE and PMRT-LBE are larger than those at the inlet, which is due to the compressible effect existing in these models. By contrast, the maximum velocities at the inlet and the outlet are almost identical from the results simulated by the IPMRT-LBE model, which demonstrates that the present model can reduce the compressible effect.

TABLE I. Comparison of three preconditioned LBE models: normalized maximum velocity at the inlet and outlet.

γ model	PSRT-LBE	PMRT-LBE	IPMRT-LBE
0.1	1.0570/1.0577	1.0570/1.0577	0.9990/0.9990
0.01	5.7116/5.7451	5.7116/5.7451	0.9991/0.9991

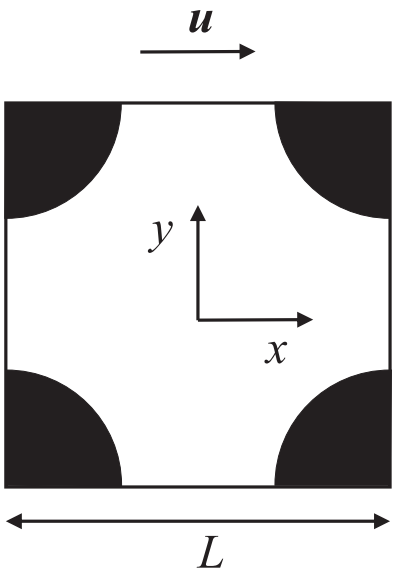

FIG. 4. 2D computational domain: circular cylinders in square array.

B. Flows in two- and three-dimensional synthetic porous media

The accuracy and the overall performance of the IPMRT-LBE model has been demonstrated via a simple test case in the previous section. We now employ this model to predict the permeability of synthetic porous media [selected representative element volume (REV) with specific structures]. A comparative study on the performance of the three models is again conducted. As known, at the REV scale, flow in porous media with low Reynolds number can be described by Darcy's law [32] as

$$\boldsymbol{u}_d = \frac{K}{\mu}(-\nabla P + \boldsymbol{G}), \tag{16}$$

where $\boldsymbol{u}_d$ is the Darcy velocity defined as the volume averaged velocity in the flow field, μ is the dynamic viscosity of the fluid, P represents the pressure, and $\boldsymbol{G}$ is the external force. Thus the permeability (K) can be calculated as

$$K = \frac{\mu u_d}{-\partial_\alpha P + G_\alpha}, \tag{17}$$

where u_d and G_α are the Darcy velocity and force in the α (i.e., x, y, z) direction, respectively.

1. Square array of cylinders

The computational domain of the 2D test case is shown in Fig. 4. For porosity close to 1, the permeability of this REV can be calculated analytically [32] as

$$K_a = \frac{d^2}{32c}[-\ln c - 1.476 + 2c - 1.774c^2 + 4.706c^3], \tag{18}$$

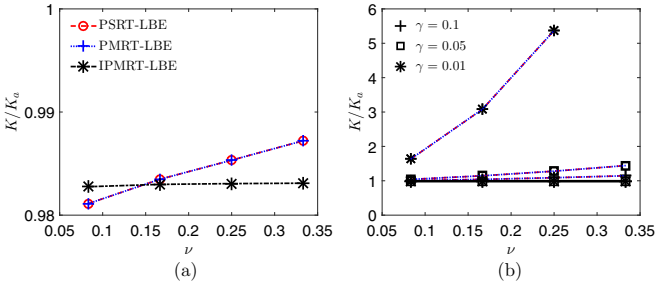

FIG. 5. Flow in 2D porous media: computed permeabilities (K/K_a) for fluids with different viscosities (ν). (a) Comparison among three models for $\gamma = 1$; (b) tests on different preconditioning factors γ (red dashed: PSRT-LBE; blue dotted: PMRT-LBE; black solid: IPMRT-LBE; black symbols: γ).

where K_a denotes the analytical permeability, $d = 2a$ is the diameter of the cylinder, where a is the radius, c is the solid volume fraction calculated as $c = \pi d^2/4H^2$, and $\phi = 1.0 - c$ is the porosity.

In our simulations, L is taken as 200, and $d = 41$, leading to a porosity of 0.967. The flow is driven by a constant external force in the x direction with $\mathrm{Re} = u_d d/\nu = 0.1$. No-slip boundary conditions are imposed at the fluid-solid interface, which are implemented using the well-known bounce-back scheme. In addition, periodic boundary conditions are employed on all the other boundaries. Simulations are conducted on 200×200 uniform lattices, which is the same as the case in Ref. [3]. The relaxation factors are selected in different ways among models: (1) in the PSRT-LBE model, the relaxation factor is determined by the fluid viscosity; (2) $s_0 = s_1 = s_2 = s_3 = s_5 = 1.0$, $s_4 = s_6 = s_7 = s_8 = 1/\tau_\nu$ in the PMRT-LBE model; (3) $s_0 = s_1 = s_2 = s_3 = s_5 = 1.0$, $s_7 = s_8 = 1/\tau_\nu$, $s_4 = s_6 = [16\tau_\nu - 8]/[8\tau_\nu - 1]$ in the IPMRT-LBE model. The convergence criterion in this case is expressed as

$$\frac{\sum_{ij} |\boldsymbol{u}(\boldsymbol{x}, t + 100\delta_t) - \boldsymbol{u}(\boldsymbol{x}, t)|}{\sum_{ij} |\boldsymbol{u}(\boldsymbol{x}, t + 100\delta_t)|} < 10^{-6}. \tag{19}$$

Simulated permeabilities from all three models (PSRT-LBE, PMRT-LBE, and IPMRT-LBE) are presented in Fig. 5. We first consider the special case with $\gamma = 1$ (without the preconditioning). As shown in Fig. 5(a), for PSRT-LBE and PMRT-LBE, K increases with fluid viscosity, which is unphysical. By contrast, the present IPMRT-LBE model can provide a physical, viscosity-independent permeability. The relative errors between the numerical results from the IPMRT-LBE model and the analytical solutions are quite minimal (less than 2%), confirming the accuracy of the present model. By comparing cases with different γ [Fig. 5(b)], we can also observe that the smaller the γ, the larger error of the results from the PSRT-LBE and PMRT-LBE model. It is reasonable because when γ gets smaller, the viscosity-related relaxation time in the PSRT-LBE and PMRT-LBE model also becomes larger, leading to a larger slip velocity at the fluid-solid interface. On the other hand, since the slip velocity is reduced in the IPMRT-LBE model by choosing the optimum relaxation factors to correctly implement the no-slip boundary condition, K computed from this model varies little for different γ.

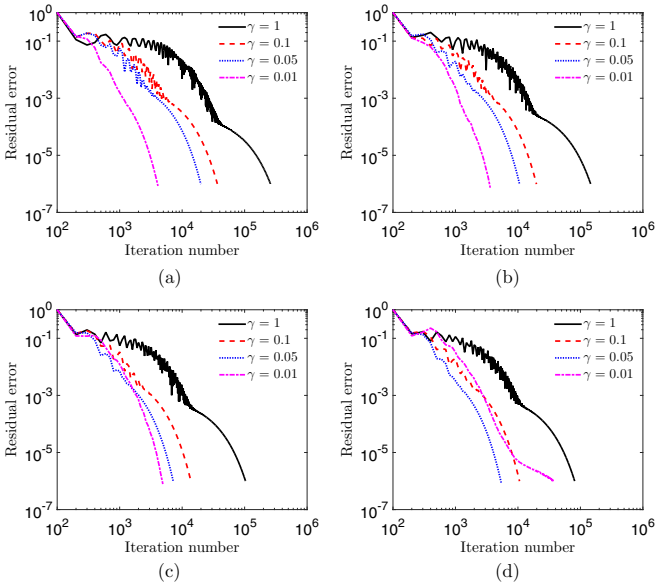

FIG. 6. Flow in 2D porous media simulated by the IPMRT-LBE: convergence histories for fluids with different viscosities (ν). Different values of the preconditioning factor γ are also tested. (a) $\nu = 1/12$; (b) $\nu = 1/6$; (c) $\nu = 1/4$; (d) $\nu = 1/3$.

In addition, the PSRT-LBE and PMRT-LBE models become numerically unstable for $\nu \approx 0.333$ as $\gamma = 0.01$ due to the large relaxation time, which is not included in Fig. 5. However, the IPMRT-LBE model can still provide an accurate permeability, suggesting the superior numerical stability of the present model.

The impact of γ on the convergence rate of the IPMRT-LBE model is further tested. As shown in Figs. 6(a)–6(c), reducing the magnitude of γ can enhance the convergence rate. As γ gets close to 0.01, the number of iterations decreases about two orders of magnitude (from 10^5 to 10^3) as compared with the case $\gamma = 1$ (standard LBE models). Also, the residual error is observed to fluctuate significantly in the convergence process as $\gamma = 1$, which would slow down the convergence rate. Those oscillations are noticed to decrease with smaller γ demonstrating the effect of preconditioning, which disappear in the cases with $\gamma = 0.01$.

It is also interesting to find that the iteration number varies nonmonotonously with γ for the case $\nu = 1/3$ [Fig. 6(d)], i.e., it first decreases with γ, then rises up. According to Eqs. (11) and (12), the smaller the γ, the larger the viscosity-related relaxation time for the same viscosity, suggesting that the following relaxation factor $\tau_q = 1/s_q$ is very close to 0.5. It may make the residual error fluctuate and thus slow down the convergence rate. Therefore, the value of the preconditioning factor (γ) should be carefully determined to ensure both the numerical stability and the convergence rate. In summary, results from 2D cylinder-array simulations indicate that the present IPMRT-LBE model can accelerate the convergence rate while retaining the accuracy and enhancing the numerical stability.

2. Body-centered cubic array of spheres

As shown in Sec. III B 1, the PSRT-LBE and PMRT-LBE models cannot provide a satisfied prediction of the perme-

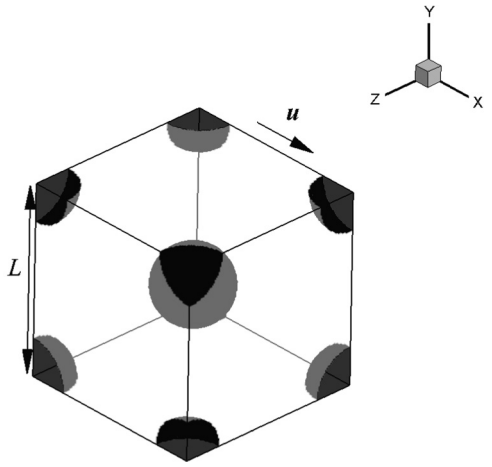

FIG. 7. 3D computational domain: periodic body-centered cubic array of spheres.

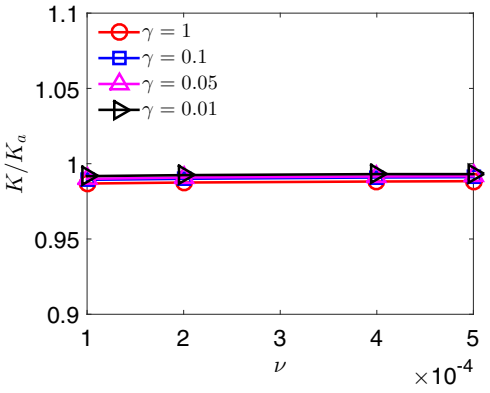

FIG. 8. Flow in 3D porous media simulated by the IPMRT-LBE: Computed permeabilities (K/K_a) for fluids with different viscosities (ν). Different values of the preconditioning factor γ are also tested.

ability even for 2D cases. Therefore, only the IPMRT-LBE is adopted for 3D simulations. The selected REV is a periodic body-centered cubic (bcc) array of spheres with equal radius a, as displayed in Fig. 7. The permeability of this REV can be expressed analytically as in [23,33,34]

$$K_a = \frac{L^3}{12\pi a d^*}, \tag{20}$$

where K_a is the analytical solution for permeability and L is the length of the cubic. In addition, d^* is the dimensionless drag, which reads as

$$d^* = \sum_{n=0}^{30} \alpha_n \chi^n, \quad \chi = \left(\frac{c}{c_{\max}}\right)^{1/3}, \tag{21}$$

$$c = \frac{8\pi a^3}{3L^3}, \quad c_{\max} = \frac{\sqrt{3}\pi}{8}, \tag{22}$$

where c is the volume fraction of the solid phase and the coefficients α_n can be found in Ref. [33].

In our simulations, L is set to be 1.0 and a is taken to be 0.2, leading to a porosity of 0.933. Flows are driven by a constant external force in the x direction with $\mathrm{Re} = 2u_d a/\nu = 0.1$. Boundary conditions and their implementations are all kept the same as in Sec. III B 1 for IPMRT-LBE. Simulations are conducted on 128^3 uniform lattices, which is fine enough to provide grid-independent results [23]. To ensure the accurate implementation of the no-slip boundary, the relaxation factors s_q are specified as $[16\tau_\nu - 8]/[8\tau_\nu - 1]$, while other relaxation factors used here are as follows: $s_{16} = s_{17} = s_{18} = s_q$, $s_3 = s_5 = s_7 = 1$, and the remaining factors are set as $s_i = 1/\tau_\nu$ [23]. The convergence criterion is also the same as in 2D simulations.

As we can see in Fig. 8, the calculated permeabilities for all cases agree well with the analytical solutions (less than 2% error), which demonstrates the accuracy of the IPMRT-LBE model for simulations of three-dimensional flows. It is also noted that the permeabilities calculated by the present model are independent of the fluid viscosity, which is consistent with the results from the 2D case. The effect of γ on the convergence rate is also evaluated as shown in Fig. 9, which again shows that reducing γ could significantly accelerate the convergence process.

We further simulate the flow as $a = \sqrt{3}/4$, in which the spheres are in contact with each other. The porosity of this structure is about 0.32. The calculated permeabilities are displayed in Fig. 10(a), which again confirms the accuracy of the present model. The effect of γ on the convergence rate is also studied. For simplicity, only the results for $\nu = 1.0 \times 10^{-4}$ are shown [Fig. 10(b)]. It can be seen clearly that reducing γ can accelerate the convergence rate.

By simulating flows in synthetic REVs (Secs. III B 1 and III B 2), the results and the associated analysis indicate that the IPMRT-LBE model can keep the advantages of previous preconditioning LBE models (such as accelerating the convergence rate) and overcome the defect of the viscosity-

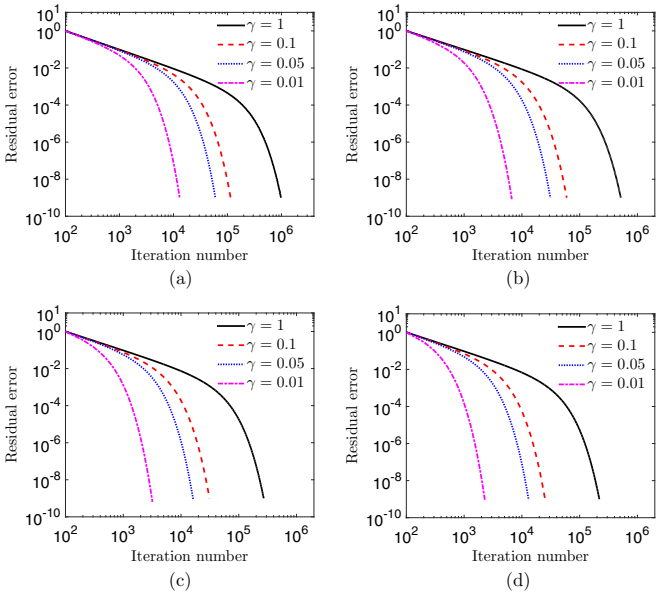

FIG. 9. Flow in 3D porous media simulated by the IPMRT-LBE: convergence histories for fluids with different viscosities (ν). (a) $\nu = 1.0 \times 10^{-4}$; (b) $\nu = 2.0 \times 10^{-4}$; (c) $\nu = 4.0 \times 10^{-4}$; (d) $\nu = 5.0 \times 10^{-4}$.

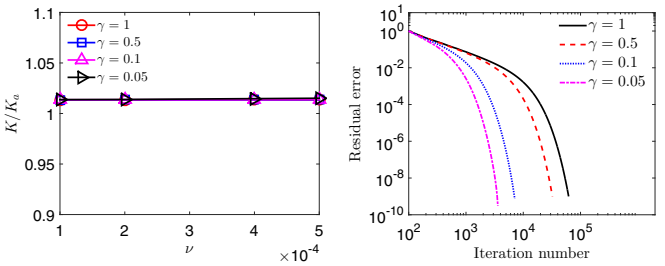

FIG. 10. Flow in touching spheres simulated by the IPMRT-LBE. (a) Computed permeabilities (K/K_a) for fluids with different viscosities (ν); (b) convergence histories for $\nu = 1.0 \times 10^{-4}$.

dependent permeability existing in the PSRT-LBE and PMRT-LBE models. In general, the IPMRT-LBE model provides accurate predictions of the macroscopic properties while maintaining the numerical stability for a wide range of model parameters.

C. Flow through rock samples

To utilize the current IPMRT-LBE model and further test its performance, flows through two different rock samples (i.e., Sandpack LV60A and F42A) with more complex structures are simulated. The rock samples used in this section are the same as the one adopted in Ref. [5], which is reconstructed from micro-CT images with the same resolutions of 10 μm. In addition, both rock samples have 300^3 voxels. The directional permeabilities for these two samples have been numerically computed using the FDM in Ref. [5], which are then served as the reference solutions here.

The structures of the rock samples are displayed in Fig. 11. We first introduce the simulations for flow in LV60A. This sandpack has a size of 3 mm × 3 mm × 3mm and a porosity of 0.377. The flow is driven by a constant external force in the x directions ($\mathrm{Re} = u_d L/\nu \approx 0.1$). No-slip boundary conditions are imposed at the fluid-solid interface, while

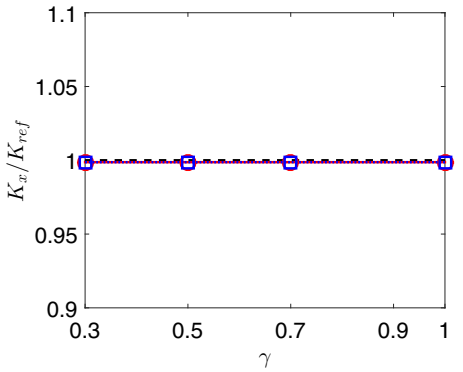

FIG. 12. Computed permeabilities for flows through the Sandpack LV60A (solid: $\nu = 2 \times 10^{-5}$; dotted: $\nu = 5 \times 10^{-5}$).

periodic boundary conditions are employed on all the other boundaries. In the present simulations, only two representative fluids, i.e., $\nu = 2 \times 10^{-5}$ and 5×10^{-5}, are employed ($L = 1.0$). Relaxation factors adopted here are the same as those used in Sec. III B 2. Due to the defect of viscosity-dependent permeability, results simulated by the PSRT-LBE and PMRT-LBE models are not included. Only IPMRT-LBE is employed for modeling. Our simulations are conducted on uniform lattices (300 × 300 × 300), following the same resolution of the image voxels.

The computed permeabilities (i.e., K_x) for different preconditioning factors are displayed in Fig. 12, which are in good agreement with the results in Ref. [5]. It is also observed that the permeabilities predicted by the present model vary little for different values of fluid viscosities and γ, which confirms the accuracy as well as the robustness of the present model. The convergence histories are displayed in Fig. 13. It can be observed that cases using preconditioning (with $\gamma < 1$) can accelerate the convergence rate as compared with the standard LBE models ($\gamma = 1$). Specifically, (1) for $\nu = 2 \times 10^{-5}$, the iteration number decreases with decreasing γ. The case with $\gamma = 0.3$ can speed up about four times as

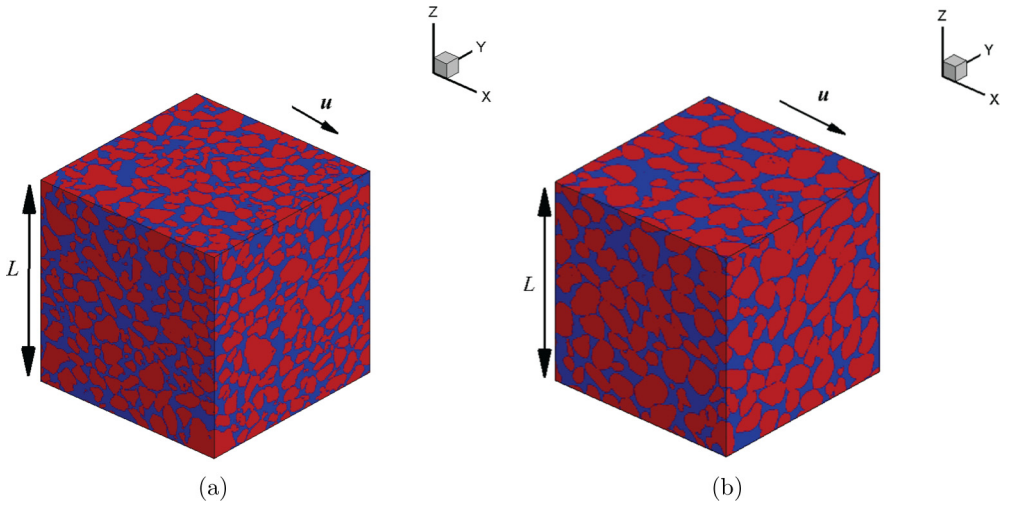

FIG. 11. Pore structure of the sandpack [5] (red: solid phase; blue: void space). (a) LV60A; (b) F42A.

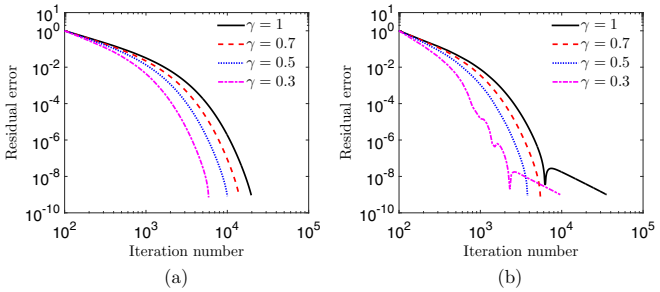

FIG. 13. Convergence histories for flows through LV60A. (a) $\nu = 2 \times 10^{-5}$; (b) $\nu = 5 \times 10^{-5}$.

compared to $\gamma = 1$. (2) As for the case $\nu = 5 \times 10^{-5}$, it is found that the iteration number first decreases with γ, then rises up. The case with $\gamma = 0.5$ can speed up about 10 times of the convergence rate as compared to $\gamma = 1$. However, the case with $\gamma = 0.3$ can only speed up about four times. It is noticed that the fluctuations exist in the convergence processes in the cases with $\gamma = 0.3$ and 1, leading to a slower convergence rate, while no fluctuations are observed in the cases with $\gamma = 0.5$ and 0.7. It is worth mentioning that similar results can also be found in Secs. III A and III B 1, which will not be analyzed in detail here.

Numerical results for flow in F42A (with a porosity of 0.33) are further summarized in Fig. 14. The computed permeabilities are again found to agree well with the reference solutions. Meanwhile, the permeabilities are observed to be independent with γ and the fluid viscosities, which can be attributed to the accurate implementation of the no-slip boundary condition in the present model. In addition, the convergence histories for $\nu = 5 \times 10^{-5}$ are also plotted, which is quite similar to the case for LV60A with $\nu = 2.0 \times 10^{-5}$, i.e., reducing γ can enhance the convergence rate.

In general, reducing γ can enhance the convergence rate in simulating porous flows. However, a too small γ may cause fluctuations in the convergence processes as shown in Secs. III A, III B 1, and III C, which may slow down the convergence rate. The threshold value of γ that causes the fluctuations strongly depends on the pore structure. To achieve a fast convergence rate for simulating porous flows, relatively larger γ ($\gamma < 1$) are suggested as fluctuations are observed in the convergence process.

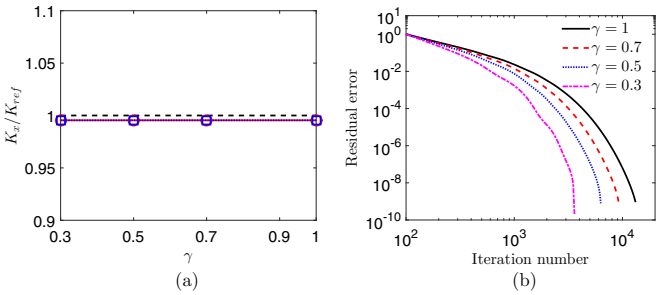

FIG. 14. Computed permeabilities and convergence histories for flows through F42A. (a) $\nu = 2 \times 10^{-5}$; dotted: $\nu = 5 \times 10^{-5}$; (b) $\nu = 5 \times 10^{-5}$.

IV. CONCLUSION

A preconditioned multiple-relaxation-time lattice Boltzmann equation model for simulating incompressible flow in porous media (IPMRT-LBE) is proposed and evaluated. This model is capable of reducing the compressible effect as compared with the previous preconditioning LBE models (PSRT-LBE and PMRT-LBE). In addition, theoretical analysis ensures the accurate implementation of the no-slip boundary condition in the current model. Thus the present IPMRT-LBE model overcomes the defect of the viscosity-dependent permeability existing in the PSRT-LBE and PMRT-LBE models. Finally, since the present model contains the preconditioning in the EDFs, it significantly accelerates the convergence rate of the simulations for flow in porous media. To validate the model, numerical simulations of the pressure-driven flows through 2D fracture demonstrate the accuracy of the IPMRT-LBE. Furthermore, simulations of flows through both two- and three-dimensional synthetic porous media show that the present model can obtain a viscosity-independent permeability with superior numerical stability. As an application, flow through a digital sandpack confirms the capability of the IPMRT-LBE model for simulating flows through realistic porous media. The preconditioning included in this model can enhance the convergence rate by orders of magnitude by adjusting the preconditioning parameter depending on the problem. In summary, considering both its efficiency as well as the accuracy, the present IPMRT-LBE model is expected to be a useful tool in studying flow and transport in porous media.

ACKNOWLEDGMENTS

X.M. and X.Y. are funded by the National Natural Science Foundation of China (Grant No. 41877183), the Recruitment Program of Global Experts in China, and the Special program for Applied Research on Super Computation of the NSFC-Guangdong Joint Fund (the second phase). Z.G. is funded by the National Natural Science Foundation of China (Grant No. 51836003). L.W. is funded by the National Natural Science Foundation of China (Grant No. 51776068). The authors would like to express their thanks to Chunhua Zhang and Professor Zhenhua Chai for fruitful discussions.

APPENDIX A: CHAPMANN-ENSKOG ANALYSIS OF THE PRESENT IPMRT-LBE MODEL

In this section, the two-dimensional preconditioned Navier-Stokes equations are derived from the present IPMRT-LBE model through the Chapman-Enskog expansion analysis. The following multiscale expansions are first employed as

$$m_i = m_i^{(0)} + \varepsilon m_i^{(1)} + \varepsilon^2 m_i^{(2)} + \cdots, \tag{A1}$$

$$\partial_t = \varepsilon \partial_{t_0} + \varepsilon^2 \partial_{t_1}, \quad \nabla = \varepsilon \nabla_0, \tag{A2}$$

where ε is a small parameter and m_i is the distribution function for pressure in the moment space.

Applying the Taylor expansion to Eqs. (4), and rewriting them in the moment space, we can obtain

$$\boldsymbol{D}\boldsymbol{m} + \frac{\delta_t}{2}\boldsymbol{D}^2\boldsymbol{m} = -\frac{\boldsymbol{S}}{\delta_t}[\boldsymbol{m} - \boldsymbol{m}^{(\mathrm{eq})}], \tag{A3}$$

where $\boldsymbol{D} = \partial_t \boldsymbol{I} + \boldsymbol{C}_{\boldsymbol{\alpha}} \partial_{\boldsymbol{\alpha}}$, in which $\boldsymbol{I}$ is the unit matrix and $\boldsymbol{C}_{\boldsymbol{\alpha}}$ is the discrete velocity matrix.

Substituting Eqs. (A1) and (5) into (A3), we can obtain the following equations in different order of ε:

$$\varepsilon^0 : \boldsymbol{m}^{(0)} = \boldsymbol{m}^{eq}, \tag{A4a}$$

$$\varepsilon^1 : \boldsymbol{D}_0 \boldsymbol{m}^{(0)} = -\frac{\boldsymbol{S}}{\delta_t}[\boldsymbol{m}^{(1)} - \boldsymbol{m}^{(1)}] + \boldsymbol{F}^{(1)}, \tag{A4b}$$

$$\varepsilon^2 : \partial_{t1} \boldsymbol{m}^{(0)} + \boldsymbol{D}_0 \boldsymbol{m}^{(1)} + \frac{\delta_t}{2} \boldsymbol{D}_0^2 \boldsymbol{m}^{(0)} = -\frac{\boldsymbol{S}}{\delta_t} \boldsymbol{m}^{(2)}, \tag{A4c}$$

where $\boldsymbol{D}_0 = \partial_{t_0} \boldsymbol{I} + \boldsymbol{C}_\alpha \partial_{0\alpha}$. Substituting Eq. (A4b) into the left-hand side of Eq. (A4c) we can obtain

$$\partial_{t1} \boldsymbol{m}^{(0)} + \boldsymbol{D}_0 \left(\boldsymbol{I} - \frac{\boldsymbol{S}}{2} \right) \boldsymbol{m}^{(1)} + \boldsymbol{D}_0 \left[\frac{\boldsymbol{S}}{2} \boldsymbol{m}^{(1)} \right] + \frac{\delta_t}{2} \boldsymbol{D}_0 \boldsymbol{F}^{(1)} = -\frac{\boldsymbol{S}}{\delta_t} \boldsymbol{m}^{(2)}. \tag{A5}$$

In addition, from Eq. (A4a) we can derive

$$j_x^{(k)} = j_y^{(k)} = 0, \quad k > 0. \tag{A6}$$

Then on the t_0 time scale, Eq. (A4b) can be rewritten as follows:

$$\partial_{0x} u + \partial_{0y} v = 0, \tag{A7a}$$

$$\partial_{t_0}[(6P + 3\boldsymbol{u}^2/\gamma)] = -\frac{s_1}{\delta_t} e^{(1)} + 6\left(1 - \frac{s_1}{2}\right) \boldsymbol{u} \cdot \boldsymbol{F}^{(1)}/\gamma, \tag{A7b}$$

$$\partial_{t0} u + \partial_{0x}(P + u^2/\gamma) + \partial_{0y}(uv/\gamma) = F_x^{(1)}, \tag{A7c}$$

$$\partial_{t0} v + \partial_{0x}(uv/\gamma) + \partial_{0y}(P + v^2/\gamma) = F_y^{(1)}, \tag{A7d}$$

$$\partial_{t0}[(u^2 - v^2)/\gamma] + \partial_{0x}\left(\frac{2}{3}u\right) + \partial_{0y}\left(\frac{-2}{3}v\right) = -\frac{s_7}{\delta_t} p_{xx}^{(1)} + 2\left(1 - \frac{s_7}{2}\right)\left[u F_x^{(1)} - v F_y^{(1)}\right]/\gamma, \tag{A7e}$$

$$\partial_{t0}(uv) + \partial_{0x}\left(\frac{1}{3}v\right) + \partial_{0y}\left(\frac{1}{3}u\right) = -\frac{\lambda_8}{\delta_t} p_{xy}^{(1)} + \left(1 - \frac{s_8}{2}\right)\left[u F_{ay}^{(1)} + v F_{ax}^{(1)}\right]/\gamma. \tag{A7f}$$

Similarly, Eq. (A4c) can be rewritten on the t_1 time scale as

$$\partial_{t1} u + \frac{1}{6}\left(1 - \frac{s_1}{2}\right)\partial_{0x} e^{(1)} + \left(1 - \frac{s_7}{2}\right)\left[\frac{1}{2}\partial_{0x} p_{xx}^{(1)} + \partial_{0y} p_{xy}^1\right] + \frac{\delta_t}{2}\left\{\partial_{0x}\left[\left(1 - \frac{s_1}{2}\right)\boldsymbol{u} \cdot \boldsymbol{F}^{(1)} + \left(1 - \frac{s_7}{2}\right)\left(u F_x^{(1)} - v F_y^{(1)}\right)\right]\right.$$
$$\left. + \partial_{0y}\left[\left(1 - \frac{s_7}{2}\right)\left(u F_{ay}^{(1)} + v F_{ax}^{(1)}\right)\right]\right\} \Big/ \gamma = 0, \tag{A8a}$$

$$\partial_{t1} v + \left(1 - \frac{s_8}{2}\right)\left[\partial_{0x} p_{xy}^1 - \frac{1}{2}\partial_{0y} p_{xx}^{(1)}\right] + \frac{1}{6}\left(1 - \frac{s_1}{2}\right)\partial_{0y} e^{(1)} + \frac{\delta_t}{2}\left\{\partial_{0x}\left[\left(1 - \frac{s_8}{2}\right)\left(u F_y^{(1)} + v F_x^{(1)}\right)\right]\right.$$
$$\left. + \partial_{0y}\left[\left(1 - \frac{s_1}{2}\right)\boldsymbol{u} \cdot \boldsymbol{F}^{(1)} - \left(1 - \frac{s_8}{2}\right)\left(u F_x^{(1)} - v F_y^{(1)}\right)\right]\right\} \Big/ \gamma = 0. \tag{A8b}$$

Moreover, we can obtain the following expression under the low Mach number assumption:

$$\partial_{t_0}(u_i u_j)/\gamma = -u_j \partial_{0i} P - u_i \partial_{0j} P + u_i F_j^{(1)} + u_j F_i^{(1)}. \tag{A9}$$

With the help of Eq. (A9), Eqs. (A7b), (A7e), and (A7f) can be expressed as

$$-\frac{s_1 e^{(1)}}{\delta_t} = 2(\partial_{0x} u + \partial_{0y} v) + 3 s_1 \boldsymbol{u} \cdot \boldsymbol{F}^{(1)}/\gamma, \tag{A10a}$$

$$-\frac{s_7 p_{xx}^{(1)}}{\delta_t} = \frac{2}{3}(\partial_{0x} u - \partial_{0y} v) + \lambda_7\left(u F_x^{(1)} - v F_y^{(1)}\right)/\gamma, \tag{A10b}$$

$$-\frac{s_8 p_{xy}^{(1)}}{\delta_t} = \frac{1}{3}(\partial_{0x} v - \partial_{0y} u) + \frac{s_8}{2}\left(u F_y^{(1)} + v F_x^{(1)}\right)/\gamma. \tag{A10c}$$

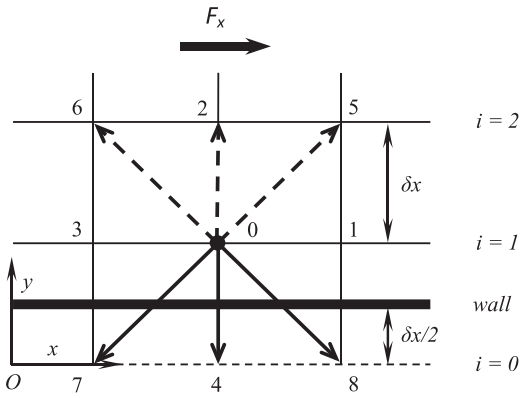

FIG. 15. Schematic of force driven flow and lattice arrangement.

Substituting Eq. (A10) into Eqs. (A8a) and (A8b), we can obtain that

$$\partial_{t1}u = \partial_{0x}\left[c_s^2\left(\frac{1}{s_1}-\frac{1}{2}\right)\delta_t(\partial_{0x}u+\partial_{0y}v)\right] + \partial_{0x}\left[c_s^2\left(\frac{1}{s_7}-\frac{1}{2}\right)\delta_t(\partial_{0x}u-\partial_{0y}v)\right] + \partial_{0y}\left[c_s^2\left(\frac{1}{s_8}-\frac{1}{2}\right)\delta_t(\partial_{0x}v+\partial_{0y}u)\right], \quad \text{(A11a)}$$

$$\partial_{t1}v = \partial_{0x}\left[c_s^2\left(\frac{1}{s_8}-\frac{1}{2}\right)\delta_t(\partial_{0x}u+\partial_{0y}v)\right] + \partial_{0y}\left[c_s^2\left(\frac{1}{s_7}-\frac{1}{2}\right)\delta_t(\partial_{0y}v-\partial_{0x}u)\right] + \partial_{0y}\left[c_s^2\left(\frac{1}{s_1}-\frac{1}{2}\right)\delta_t(\partial_{0x}u+\partial_{0y}v)\right]. \quad \text{(A11b)}$$

Coupling the equations on the t_0 and t_1 scale, the macroscopic equations (1) can be obtained.

APPENDIX B: ON THE ACCURATE IMPLEMENTATION OF THE NO-SLIP BOUNDARY CONDITION

Previous studies have indicated that the relaxation factors (e.g., s_4) have significant influences on the precise implementation of the no-slip boundary condition. Therefore, the choice of the relaxation factors in the present IPMRT-LBE model will be analyzed in this section.

As shown in Fig. 15, we consider a steady incompressible Poiseuille flow driven by a constant force $\boldsymbol{F} = \rho(F_x, 0)$ for simplicity, in which we assume that

$$\frac{\partial\psi}{\partial t} = 0, \quad \rho = \text{const}, \quad u_y = 0, \quad \frac{\partial\psi}{\partial x} = 0, \quad \text{(B1)}$$

where ψ is an arbitrary flow variable.

We can first obtain the following equations based on the relationship between $\boldsymbol{f}$ and $\boldsymbol{m}$ at the node $i = 1$:

$$f_1^1 - f_3^1 = \tfrac{1}{3}j_x^1 - \frac{1}{3}q_x^1, \quad \text{(B2)}$$

$$f_5^1 - f_6^1 = \tfrac{1}{3}j_x^1 + \tfrac{1}{6}q_x^1 + \tfrac{1}{2}p_{xy}^1, \quad \text{(B3)}$$

$$f_8^1 - f_7^1 = \tfrac{1}{3}j_x^1 + \tfrac{1}{6}q_x^1 - \tfrac{1}{2}p_{xy}^1, \quad \text{(B4)}$$

from which we can obtain

$$j_x^1 = u_x - \frac{\delta_t}{2\gamma}F_x. \quad \text{(B5)}$$

Next, the postcollision distribution functions can also be expressed in a similar way as follows:

$$f_1'^1 - f_3'^1 = \tfrac{1}{3}j_x'^1 - \tfrac{1}{3}q_x'^1, \quad \text{(B6)}$$

$$f_5'^1 - f_6'^1 = \tfrac{1}{3}j_x'^1 + \tfrac{1}{6}q_x'^1 + \tfrac{1}{2}p_{xy}'^1, \quad \text{(B7)}$$

$$f_8'^1 - f_7'^1 = \tfrac{1}{3}j_x'^1 + \tfrac{1}{6}q_x'^1 - \tfrac{1}{2}p_{xy}'^1, \quad \text{(B8)}$$

where ψ' ($\psi = f, q, p$) are the postcollision distribution functions. Meanwhile, the postcollision distribution functions in the moment space in Eqs. (B6)–(B8) can be obtained from Eq. (4) as

$$j_x'^1 = (1-s_3)j_x^1 + s_3u_x + \left(1-\frac{s_3}{2}\right)F_x\delta_t/\gamma, \quad \text{(B9)}$$

$$q_x'^1 = (1-s_4)q_x^1 - s_4u_x - \left(1-\frac{s_4}{2}\right)F_x\delta_t/\gamma, \quad \text{(B10)}$$

$$p_{xy}'^1 = (1-s_8)p_{xy}^1. \quad \text{(B11)}$$

Then, substituting Eq. (B5) into Eq. (B9), we can obtain that

$$j_x'^1 = u_x + \frac{F_x\delta_t}{2\gamma}. \quad \text{(B12)}$$

In addition, we can get the following relationship from the unidirectional property of the flow:

$$f_1^1 - f_3^1 = f_1'^1 - f_3'^1. \quad \text{(B13)}$$

Combining Eqs. (B2), (B5), (B6), (B10), and (B12), we can obtain that

$$q_x^1 = -u_x - \left(\frac{2}{s_4}-\frac{1}{2}\right)F_x\delta_t/\gamma, \quad \text{(B14)}$$

$$q_x'^1 = -u_x - \left(\frac{2}{s_4}-\frac{3}{2}\right)F_x\delta_t/\gamma. \quad \text{(B15)}$$

It is noted that the relationship between the distribution functions at $i = 1$ and $i = 2$ are

$$f_5^2 - f_6^2 = f_5'^1 - f_6'^1, \quad f_8^1 - f_7^1 = f_8'^2 - f_7'^2. \quad \text{(B16)}$$

Similarly, substituting Eqs. (B3), (B4), (B7), and (B8) into (B16), we can obtain the expression of p_{xy}^1 as follows:

$$p_{xy}^1 = \frac{[(2/s_8-1)(u_1-u_2) - 3F_x\delta_t/\gamma]}{3(2-s_8)}, \quad \text{(B17)}$$

and then $p_{xy}'^1$ can also be obtained with the help of Eq. (B11). Furthermore, we can also obtain the following relationship as the bounce-back scheme is adopted:

$$f_5^1 - f_6^1 = f_7'^1 - f_8'^1. \quad \text{(B18)}$$

With these results at hand, the relationship between u_2 and u_1 can now be obtained as follows:

$$u_2 = 3u_1 + \left[2 - 4\tau_q - \frac{3}{2(\tau_v-0.5)}\right]F_x\delta_t/\gamma, \quad \text{(B19)}$$

where $\tau_q = 1.0/s_4 = 1.0/s_6$ and $\tau_v = 1.0/s_7 = 1.0/s_8$.

As for the steady Poiseuille flow considered here, the velocity can be written as

$$u_i = 4u_c \frac{y_i}{L}\left(1 - \frac{y_i}{L}\right) + u_s, \quad i = 1, 2, \tag{B20}$$

where $y_i = (i - 0.5)\delta_x$, $u_c = F_x L^2/8\nu$, and u_s represents the slip velocity resulting from the bounce-back boundary condition. Substituting Eq. (B20) into Eq. (B19), we can obtain the dimensionless slip velocity

$$U_s = \frac{u_s}{u_c} = \frac{16(\tau_q - 0.5)(\tau_\nu - 0.5) - 3}{3}\Delta^2, \tag{B21}$$

where $\Delta = \delta_x/L$, and U_s can be zero if τ_q is chosen as $[8\tau_\nu - 1]/[16\tau_\nu - 8]$. Thus the corresponding relaxation rates s_4 and s_6 in the present model to satisfy the no-slip boundary condition are

$$s_4 = s_6 = \frac{16\tau_\nu - 8}{8\tau_\nu - 1}. \tag{B22}$$

For the D3Q19 model, we can also obtain the following equations:

$$s_4 = s_6 = s_8 = \frac{16\tau_\nu - 8}{8\tau_\nu - 1}, \tag{B23}$$

to ensure the precise implementation of the no-slip boundary condition in 3D. Finally, it is worth mentioning that the relaxation factor which can ensure the accurate implementation of the no-slip boundary condition on inclined walls can also be obtained in a similar way. More related information can be found in Refs. [28–30].

[1] H. Yoon, Q. Kang, and A. J. Valocchi, Rev. Mineral. Geochem. **80**, 393 (2015).
[2] Z. H. Chai, C. S. Huang, Z. L. Guo *et al.*, Int. J. Heat Mass Transfer **98**, 687 (2016).
[3] X. H. Meng and Z. L. Guo, Phys. Rev. E **92**, 043305 (2015).
[4] N. Rakotomalala, D. Salin, and P. Watzky, J. Fluid Mech. **338**, 277 (1997).
[5] P. Mostaghimi, M. J. Blunt, and B. Bijeljic, Math. Geosci. **45**, 103 (2013).
[6] X. F. Yang, T. D. Scheibe, M. C. Richmond *et al.*, Adv. Water Resour. **54**, 228 (2013).
[7] X. F. Yang, Y. Mehmani, W. A. Perkins *et al.*, Adv. Water Resour. **95**, 176 (2016).
[8] A. M. Tartakovsky and P. Meakin, J. Comput. Phys. **207**, 610 (2005).
[9] S. Molins, D. Trebotich, L. Yang *et al.*, Environ. Sci. Technol. **48**, 7453 (2014).
[10] Z. H. Chai, Z. L. Guo, and B. C. Shi, J. Appl. Phys. **101**, 104913 (2007).
[11] Z. H. Chai, B. C. Shi, J. H. Lu *et al.*, Comput. Fluids **39**, 2069 (2010).
[12] D. d'Humières and I. Ginzburg, Philos. Trans. R. Soc. London A **360**, 437 (2002).
[13] T. Inamuro, Philos. Trans. R. Soc. London A **360**, 477 (2002).
[14] X. G. Yang, B. C. Shi, and Z. H. Chai, Phys. Rev. E **90**, 013309 (2014).
[15] L. Wang, J. C. Mi, X. H. Meng *et al.*, Commun. Comput. Phys. **17**, 908 (2015).
[16] T. Krüger, H. Kusumaatmaja, A. Kuzmin *et al.*, *The Lattice Boltzmann Method: Principles and Practice* (Springer, New York, 2016).
[17] Y. G. Lai, C. L. Lin, and J. C. Huang, Numer. Heat Transfer, B **39**, 21 (2001).
[18] Z. L. Guo, T. S. Zhao, and Y. Shi, Phys. Rev. E **70**, 066706 (2004).
[19] D. Kandhai, A. Hoekstra, and P. M. A. Sloot, Future Gen. Comput. Syst. **18**, 89 (2001).
[20] T. Seta and R. Takahashi, J. Stat. Phys. **107**, 557 (2002).
[21] T. Lee and C. L. Lin, J. Comput. Phys. **185**, 445 (2003).
[22] J. Tölke, M. Krafczyk, and E. Rank, J. Stat. Phys. **107**, 573 (2002).
[23] C. Pan, L. S. Luo, and C. T. Miller, Comput. Fluids **35**, 898 (2006).
[24] K. N. Premnath, M. J. Pattison, and S. Banerjee, J. Comput. Phys. **228**, 746 (2009).
[25] L. Chen, Q. Kang, H. S. Viswanathan *et al.*, Water Resour. Res. **50**, 9343 (2014).
[26] Z. L. Guo, B. C. Shi, and N. C. Wang, J. Comput. Phys. **165**, 288 (2000).
[27] D. d'Humières and I. Ginzburg, Comput. Math. Appl. **58**, 823 (2009).
[28] L. Talon, D. Bauer, N. Gland *et al.*, Water Resour. Res. **48**, W04526 (2012).
[29] S. Khirevich, I. Ginzburg, and U. Tallarek, J. Comput. Phys. **281**, 708 (2015).
[30] G. Silva, L. Talon, and I. Ginzburg, J. Comput. Phys. **335**, 50 (2017).
[31] Z. L. Guo, C. G. Zheng, and B. C. Shi, Chin. Phys. **11**, 366 (2002).
[32] A. S. Sangani and A. Acrivos, Int. J. Multiphase Flow **8**, 193 (1982).
[33] A. S. Sangani and A. Acrivos, Int. J. Multiphase Flow **8**, 343 (1982).
[34] H. Hasimoto, J. Fluid Mech. **5**, 317 (1959).